Phantom motion of the ocean

Leakage of geometrical Doppler into geophysical motions observed with Doppler scatterometers

O'Driscoll, Owen; López-Dekker, Paco; Payez, Alexandre

DOI
10.1109/TGRS.2025.3589713

Publication date
2025

Document Version
Final published version

Published in
IEEE Transactions on Geoscience and Remote Sensing

Phantom Motion of the Ocean: Leakage of Geometrical Doppler Into Geophysical Motions Observed With Doppler Scatterometers

Owen O'Driscoll, Paco López-Dekker, *Senior Member, IEEE*, and Alexandre Payez

***Abstract*— The interactions among geometrical Doppler, beam pattern, and normalized radar cross section (NRCS) result in the unwanted coupling leakage of geometrical Doppler into the perceived geophysical Doppler. Starting from high-resolution synthetic aperture radar (SAR) data, we model this leakage for synthesized real aperture radar (RAR) observations of ocean motion. The uncertainty introduced by leakage is $\sim$1 m $\cdot$ s^{-1}. Corrections proposed in this work exploit the known interactions between beam pattern and geometric Doppler with NRCS gradients retrieved from simulated low-resolution RAR to estimate and correct for the incurred leakage, reducing the uncertainty to $\mathcal{O}$(0.1 m $\cdot$ s^{-1}). Further reduction of instantaneous leakage may be achieved through temporal averaging, since the NRCS gradients that cause leakage appear mostly atmosphere-induced and decorrelate rapidly. The azimuth resolution and number of independent samples determine a system's sensitivity to leakage. C-band systems are inherently prone to suffer from greater leakage and worse corrections than their Ku- and Ka-band counterparts. With DopSCA, the propagated effect of leakage is only secondary compared with the pulse-pair uncertainty. In similar systems where pulse-pair uncertainty is suppressed, leakage will dominate instead.**

***Index Terms*— Doppler scatterometers, DopSCA, leakage, real aperture radars (RARs), surface currents, surface motion.**

I. Introduction

THE apparent geophysical surface velocity originating from the interplay between geometrical Doppler, radar beam pattern, and normalized radar cross section (NRCS) gradients is an undesired contribution to surface-current observations that often flies under the proverbial radar. This phenomenon has primarily been studied in the context of Doppler profilers and synthetic aperture radars (SARs), where it is referred to as "nonuniform beam filling" [1], [2], [3], [4] and "biased Doppler centroids (DCs)," respectively [5], [6], [7]. Here, we will refer to it as leakage, as the geometrical Doppler seemingly leaks into the geophysical Doppler of interest, causing a phantom motion.

Received 20 January 2025; revised 20 June 2025; accepted 14 July 2025. Date of publication 16 July 2025; date of current version 28 July 2025. This work was supported by ESA under Contract 4000142633/23/NL/MGu. *(Corresponding author: Owen O'Driscoll.)*

Owen O'Driscoll and Paco López-Dekker are with the Department of Geoscience and Remote Sensing, Delft University of Technology, 2628 CN Delft, The Netherlands (e-mail: o.p.odriscoll@tudelft.nl).

Alexandre Payez is with the Royal Netherlands Meteorological Institute (KNMI), 3731 GA De Bilt, The Netherlands.

Digital Object Identifier 10.1109/TGRS.2025.3589713

A new generation of Doppler-targeting real aperture radar (RAR) missions has been proposed with the objective of mapping ocean surface motions at hitherto unattainable spatial and temporal scales, such as, e.g., SKIM [8], WaCM (rechristened as Odysea) [9], and OSCOM [10]. Such capabilities, and especially their added ability to provide direct observations of ocean surface motions at a global scale for the very first time, are needed to complement and update the mostly indirect contemporary view of ocean surface currents (OSCs) derived from space-borne altimeters (made under the assumption of large-scale geostrophic balance) and highly localized high-resolution observations (e.g., coastal HF radars, moorings, drifters, or sporadic campaigns, such as the recent ESA RVL campaign over the Aghulas) [11]. SWOT [12] will help bridge the altimetry gap, but it remains an altimeter (albeit a large-swath interferometric one), and currents demand complementary direct observations, in particular in the tropics close to the equator.

The unique design of the Doppler-targeting systems determines their inherent sensitivity to leakage. For RARs such as SKIM and Odysea, the incurred leakage is fundamentally linked to the width of the beam footprint: a wider beam enables more NRCS gradients to bias the geometric Doppler, while stronger gradients further enhance this bias. With both Odysea and SKIM operating at the Ka band, their beam footprints are much narrower than C-band equivalent systems; the anticipated leakage is therefore reduced. For DopplerScat, the airborne counterpart of Odysea, Rodríguez et al. [13] estimated the leakage-induced velocity errors to be $\mathcal{O}$(0.01 m $\cdot$ s^{-1}), though sharp NRCS gradients will result in more substantial errors and require correction. SAR platforms such as Harmony receive signals from a much wider C-band footprint [14], but the SAR-enabled azimuthal resolving power permits correction for leakage-induced Doppler. Common correction approaches rely on empirical relations [2], [3], [7], iterative procedures [15], a priori filtering [7], or spectral filtering [16], [17].

Given the seemingly benign nature of leakage to these systems, other components of the error budget justifiably take precedence, such as measurement noise, pointing errors, and uncorrected wave Doppler.

However, inauspicious combinations of system design parameters will cause a subset of sensors to be particularly prone to suffer from leakage. One of these is DopSCA: an

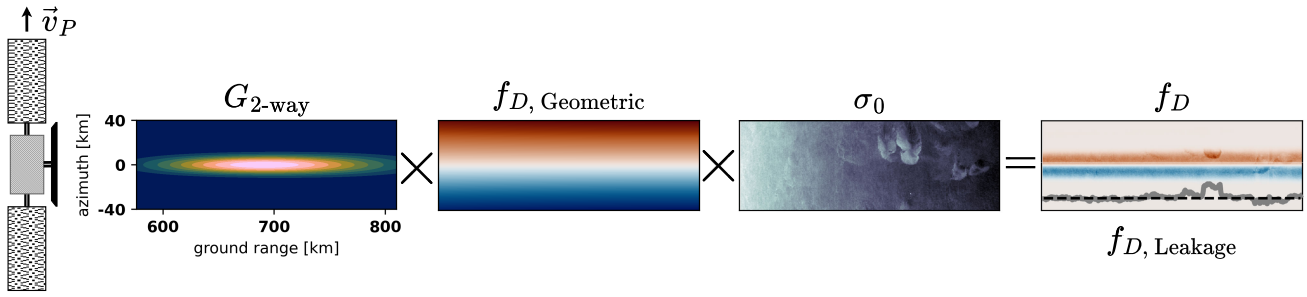

Fig. 1. Overview of the leakage mechanism for a single RAR pulse. The geometric Doppler, caused by platform motion v_p, is weighted by the beam pattern and NRCS fields, resulting in a characteristic DC, f_D. Where NRCS gradients occur, the DC's azimuthal average—here within a single azimuthal resolution cell—becomes nonzero. Under the false assumption that the geometric Doppler is symmetric and will cancel out, this phantom signal, $f_{D,\text{ Leakage}}$, could erroneously be interpreted as a geophysical motion instead.

opportunistic mission design proposed under ESA's DOPSCAT study for scatterometers capable of measuring ocean surface motions [18]. This concept is being investigated as an additional capability for the new MetOp-SG operational C-band fan-beam scatterometer instrument: SCA. With the requirement not to impede the original scatterometer performance of SCA, DopSCA targets the estimation of ocean surface velocities inferred from subpulse-pair phase differences [19].

However, constrained by prioritization given to the scatterometer mission aspect, the C-band fan-beam design—with a large azimuthal beam footprint—is inherently sensitive to leakage. As such, the previously unconsidered NRCS gradients may yet irreversibly hinder the estimation of ocean surface velocity vectors.

Thus, to assess the viability of C-band Doppler scatterometers, we must quantify their sensitivity to leakage. DopSCA will be considered as a relevant case study. First, we aim to quantify the expected leakage using high-resolution SAR observations. These provide us with high-resolution NRCS gradients. Then, we assess corrections for the incurred leakage using synthesized low-resolution scatterometer observations.

Next, we illustrate the practical implications of residuals after correction on a limited dataset with surface current estimates over the Aghulas. Finally, mitigation strategies are considered with the aim of overcoming residual leakage.

Through these analyses, we intend to answer the following questions. To what extent are Doppler scatterometers sensitive to uncertainty introduced by leakage? Can leakage be reduced to acceptable levels through correction? What alterations to the instrument/observation mechanism could aid uncertainty reduction?

II. Theory and Methodology

A. DC and Leakage Velocity

Following [20], the DC for a single range bin can be expressed as follows:

$$f_D = \frac{2}{\lambda} \frac{\int \sigma_0 \, G_{2\text{-way}} \left(\vec{v}_p - \vec{v}_s\right) \cdot \hat{r}_{\text{LoS}} \, d\text{Az}}{\int \sigma_0 \, G_{2\text{-way}} \, d\text{Az}} \tag{1}$$

where $\vec{v}_p$ is the platform velocity vector (considered constant but left inside the integral for ease of notation), $\vec{v}_s$ is the spatially varying surface motion of interest, λ is the radio wavelength, σ_0 is the spatially varying NRCS, $G_{2\text{-way}}$ is the two-way antenna gain pattern, and $\hat{r}_{\text{LoS}}$ is the line-of-sight (LoS) unit vector representing the satellite viewing geometry within the azimuthal domain represented as Az. For notational convenience, references to azimuth coordinates are dropped.

From (1), it follows that both the geometric and geophysical contributions of relative motion ($\vec{v}_p$ and $\vec{v}_s$, respectively) are weighted by the local NRCS and antenna gain. In the absence of geophysical motion, the DC is only governed by the antenna pattern, NRCS, and the observation geometry, as shown in Fig. 1. Meanwhile, in the here not considered along-track interferometry case, the platform's velocity-induced geometric Doppler drops out, because we observe the surface from the same location. For pulse-pair systems, it is necessary to explicitly estimate and remove this geometric component instead. Assuming a simplified scenario where a perfectly right-looking RAR system observes a uniform NRCS field with a symmetric beam footprint, then the even weighting of the positive and negative geometric Doppler would effectively cancel out the integral terms corresponding to $\vec{v}_p$, yielding only the LoS-average geophysical Doppler of interest. However, for more realistic scenarios containing along-azimuth σ_0 gradients within the beam footprint, more weight is given to geometric Dopplers corresponding to bright scatterers (i.e., with larger σ_0); the previously balanced geometric Doppler weighting is now distorted. One can expect compounding and nonzero interactions between σ_0 and $G_{2\text{-way}}$ and the geometric Doppler to result in spurious and undesired Doppler contributions that bias the DC leakage. This Phenomenon is illustrated in Fig. 1.

The sensitivity to σ_0 gradients is determined by the gain pattern. To calculate this sensitivity analytically, we first identify in (1) convolutions of NRCS with distinct impulse response functions in both numerator and denominator. Assuming no surface motion ($\vec{v}_s = 0$), a stationary beam pattern and geometric Doppler, and discarding changes in NRCS due to changes in viewing geometry; then, (1) can be approximated as follows:

$$f_D = \frac{2}{\lambda} \frac{(\sigma_0 * h_1)}{(\sigma_0 * h_2)} \tag{2}$$

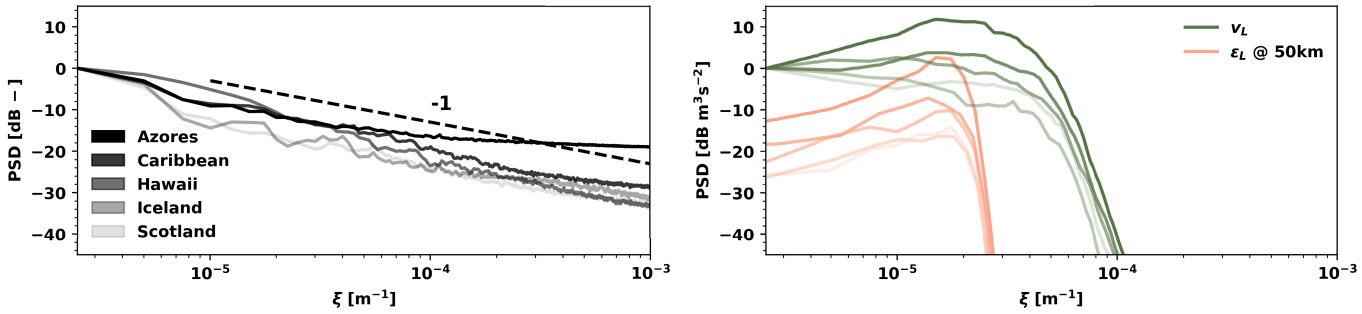

Fig. 2. (Left) Relative azimuthal power spectral densities (PSDs) of high-resolution NRCS. (Right) PSD for native resolution leakage, v_L, and residual leakage after correction, ϵ_L, averaged to a 50-km ground-projected spatial resolution. Spectra are estimated along a 400-km azimuthal section and averaged across range for each case study in Table III. Spectra of residual leakage are relative to the original leakage. The presented spectra are anecdotal but illustrate the prevailing decreasing gradients in NRCS at smaller scales as well as the consistent behavior of (residual) leakage. The sharp cutoff in residual leakage for wavenumbers beyond 2×10^{-5} m^{-1} is caused by the aforementioned spatial filtering. The spatial filtering is needed to reduce the speckle's inhibitory effect on leakage estimation. The gradual roll-off in v_L traces the beam footprint's frequency response.

with $*$ being the convolution operator and

$$h_1 = G_{2\text{-way}} \vec{v}_p \cdot \hat{r}_{\text{LoS}} \tag{3}$$

$$h_2 = G_{2\text{-way}}. \tag{4}$$

After resolving these impulse response functions in the spatial domain, the convolutions in (2) can conveniently be resolved in the azimuthal wavenumber domain as follows:

$$f_D = \frac{2}{\lambda} \frac{\mathcal{F}^{-1}(\Sigma_0 H_1)}{\mathcal{F}^{-1}(\Sigma_0 H_2)} \tag{5}$$

where $\mathcal{F}^{-1}$ indicates an inverse azimuthal Fourier transform of the product of the NRCS wavenumber domain transfer functions, Σ_0, with the respective wavenumber domain transfer functions H_1 and H_2. The expression in (5) is computationally more efficient than the convolution laden (1), with which it differs negligibly (not shown), but it hinges on the aforementioned additional assumptions.

The Doppler resulting from leakage is converted to the horizontal component of leakage velocity in the following equation:

$$v_L = \frac{\lambda}{2} \frac{f_D}{\sin(\theta_i)} \tag{6}$$

with θ_i being the incidence angle. Successive pulses retrieved at multiple range bins yields $v_L(t, \tau)$ as a function of fast and slow times, respectively.

B. Toward an Intuitive Wavenumber Interpretation, and Motivation for Empirical Analyses

From (1) and (5), several properties of leakage can already be deduced. Yet, the division of convolutions thwarts a convenient wavenumber-domain interpretation. Aiming to that end, we decompose σ_0 into a mean and space-varying component [21]

$$\sigma_0 = \bar{\sigma_0} + \bar{\sigma_0} \delta\sigma_0 \tag{7}$$

such that (2) becomes

$$f_D = \frac{2}{\lambda} \frac{\bar{\sigma_0}(h_1 * 1 + h_1 * \delta\sigma_0)}{\bar{\sigma_0}(h_2 * 1 + h_2 * \delta\sigma_0)}. \tag{8}$$

Since the mean backscatter terms cancel, and convolutions with an identity field yield the mean impulse response, i.e., $h_1(x) * 1 = H_1(0)$, we can rewrite as follows:

$$f_D = \frac{2}{\lambda} \left[\frac{H_1(0)}{H_2(0) + h_2 * \delta\sigma_0} + \frac{h_1 * \delta\sigma_0}{H_2(0) + h_2 * \delta\sigma_0} \right]. \tag{9}$$

The latter fraction can be approximated as follows:

$$\frac{h_1 * \delta\sigma_0}{H_2(0) + h_2 * \delta\sigma_0} = \frac{h_1 * \delta\sigma_0}{H_2(0)} \frac{1}{1 + x} \tag{10}$$

$$x = \frac{h_2 * \delta\sigma_0}{H_2(0)}. \tag{11}$$

Using a Taylor expansion for $(1/1 + x)$ we can linearize, yielding

$$f_D = \frac{2}{\lambda} \left[\frac{H_1(0)}{H_2(0) + h_2 * \delta\sigma_0} + \frac{h_1 * \delta\sigma_0}{H_2(0)} \cdot \left(1 - \frac{(h_2 * \delta\sigma_0)}{H_2(0)} + \frac{(h_2 * \delta\sigma_0)^2}{H_2(0)^2} - \dots \right) \right]. \tag{12}$$

This form provides insight into the effects of various magnitudes of NRCS gradients. First, based on Fig. 2, leakage will be greater for smaller wavenumbers (for the same beam impulse response) as the power of NRCS gradients decreases toward greater wavenumbers. Then, in the limit when only weak gradients are present, such that

$$\lim_{\delta\sigma_0 \to 0} (h_2 * \delta\sigma_0) = \lim_{\delta\sigma_0 \to 0} (h_1 * \delta\sigma_0) = 0 \tag{13}$$

it follows from (12) that $f_D \propto (H_1(0)/H_2(0))$, which is the geometric Doppler. Conversely, for nonzero NRCS gradients things become more complicated: the geometric Doppler term is gradually suppressed through division by $h_2 * \delta\sigma_0$, and the multiplication of various higher order terms with $h_1 * \delta\sigma_0$ leads to scale interactions across wavenumbers. For a symmetric beam and geometric Doppler, such as considered here, $H_1(0) = 0$, leaving only the terms resulting from scale interaction. The resulting spectra of v_L approach the spectrum of the corresponding beam pattern, see the right half of Fig. 2 where the shared and gradual roll-off occurs at the limit of the

TABLE I
FOLLOWING PLATFORM PARAMETERS ARE ASSUMED, RESPECTIVELY, RETRIEVED FROM: ANTENNA DIMENSIONS AND ALTITUDE [23]; ANTENNA ELEMENTS [24]; AND WAVEFORM AND DOPPLER PRODUCT PARAMETERS [19]

Parameter	Quantity
Platform altitude	823 km
Platform velocity	6800 m s^{-1}
Antenna height broadside	0.32 m
Antenna length broadside	2.87 m
Antenna elements azimuth	4
Antenna elements elevation	1
Beam footprint azimuthal truncation	80 km
Ground yaw angle	0°
Boresight elevation angle	40°
Considered swath elevation angles	35° - 45°
Wavelength	5.5 cm
Nr. of subpulses	2
Sub pulse bandwidth	1 MHz
Slant range resolution	150 m
Maximum total pulse length	1.15 ms
Time between sub-pulses	0.115 ms
Sub-pulse SNR	1
PRF at broadside	3.942 Hz[1]
Ground-projected Doppler product resolution	50 km

footprint's spatial resolution. The calculation of the presented (residual) leakage spectra will be covered later.

Despite making several simplifying assumptions, no convenient expression results from the procedures described above; to quantify f_D one still needs the fields h_1, h_2, and $\delta\sigma_0$, warranting a comprehensive approach instead.

C. Data Synthesis and Leakage Correction

Since leakage is the result of NRCS gradients, any observations of the NRCS field can be combined with a known beam pattern and geometrical Doppler to estimate the incurred leakage. We use the high-resolution Sentinel-1 NRCS and (1) to approximate the true incurred leakage. It does not matter that the Sentinel-1 NRCS has a finite resolution, as the spatial scales most prone to leakage—those at the limit of the scatterometer resolution—are well captured, see Fig. 2. Next, we synthesize a coarse scatterometer-observed NRCS with which we aim to correct for the estimated incurred leakage. The data synthesis and correction steps are detailed in Fig. 3.

Artificial fan-beam scatterometer data is synthesized by stitching together several Sentinel-1 frames along azimuth, simulating a range subset of the continuous scatterometer observations. The Sentinel-1 NRCS data ($\sigma_{0,\ \mathrm{S1}}$) is mapped to the stress equivalent winds (U_{10s}) using wind directions from ERA5, and these winds are translated back to a high-resolution DopSCA-equivalent NRCS (σ_0) using the CMOD5.N geophysical model function [22]. This compensates for their respective viewing geometries. The high spatial and radiometric resolution of σ_0 allows it to be used as a reference and starting point from which to estimate the much coarser NRCS observed by DopSCA ($\sigma_{0,\mathrm{SCA}}$) based on the parameters listed in Table I. Computations are simplified by assuming a rectilinear geometry; no squint, pitch, yaw, or roll; and neglecting any Earth-rotation effects. Furthermore, range cell migration is assumed to have been corrected for.

[1]For discretization ease, we deviate from the frequently referenced 4 Hz.

The σ_0 field is sampled at a uniform 75-m ground-range spacing $\Delta x_{\mathrm{ground}}$ to generously comply with Nyquist for DopSCA's 150-m slant-range resolution. In order to compute $\sigma_{0,\mathrm{SCA}}$, we need to momentarily convert to a uniform slant-range spacing $\Delta x_{\mathrm{slant}}$, which is equivalent to a variable ground-range projected spacing. Spacing conversions are performed with linear interpolators indicated by

$$\begin{aligned}\mathcal{A}_{g\to s} &: \Delta x_{\mathrm{ground}} \to \Delta x_{\mathrm{slant}}\\ \mathcal{A}_{s\to g} &: \Delta x_{\mathrm{slant}} \to \Delta x_{\mathrm{ground}}\end{aligned} \tag{14}$$

where the sequence of $\mathcal{A}_{g\to s}$ and $\mathcal{A}_{s\to g}$ results in a variable low-pass filtering along ground range with worse ground-range resolution for lesser elevation angles. The variable ground-range-projected slant-range spacing is computed as follows:

$$\Delta x_{\mathrm{slant}} = \frac{\Delta x_{\mathrm{ground}}}{\sin(\theta_{\mathrm{i}})}. \tag{15}$$

The simulated true value of the scatterometer-observed NRCS is computed as follows:

$$\sigma_{0,\mathrm{SCA}} = \mathcal{A}_{g\to s}\left(\frac{\int_\eta \sigma_0\, G_{2\text{-way}}\, d\mathrm{Az}}{\int_\eta G_{2\text{-way}}\, d\mathrm{Az}}\right) \tag{16}$$

which integrates the high-resolution σ_0 within the truncated azimuthal beam footprint at azimuthal intervals defined by the pulse repetition frequency (PRF). The azimuthal truncation is performed for computational reasons such that the truncated along-azimuth coverage is a constant 40 km to the front and rear of boresight represented by η in the following equation:

$$\eta = \mathrm{Az}|_{\pm 40\ \mathrm{km}} \tag{17}$$

where Az refers to the entire azimuthal extent. Increasing the truncation extent had little effect on the results. Depending on the beam pattern, a variable azimuthal truncation should be considered as a function of elevation angle.

The azimuthal component of $G_{2\text{-way}}$ can be approximated as a function of antenna length L_A [25]. Usually, tapered beam patterns are used, widening the main beam and reducing side lobes. For instance, ASCAT's sidelobes required attenuation in order to avoid signals reflecting from parts of the satellite itself [26]. Azimuthal beam tapering employed in this study increases the beamwidth of $G_{2\text{-way}}$ from 0.69° to 0.78°.

To simulate a realization of the observed NRCS, random speckle is added to the true NRCS. We model multiplicative speckle, $\mathcal{S}$, as a unit power circular-Gaussian band-limited random signal, and compute the observed NRCS as follows:

$$\hat{\sigma}_{0,\mathrm{SCA}} = \mathcal{A}_{s\to g}\left(\sigma_{0,\mathrm{SCA}} \cdot |\mathcal{S}|^2\right). \tag{18}$$

With multiplicative speckle added, the data are interpolated back to a uniform 75-m ground-range spacing.

From the observed $\hat{\sigma}_{0,\mathrm{SCA}}$ and using (1), we compute an estimate of the leakage velocity, $\hat{v}_{L,\mathrm{SCA}}$. In the case that we have no geophysical motions and the theoretical DC is 0, the difference in leakage estimated from σ_0 and $\hat{\sigma}_{0,\mathrm{SCA}}$ yields the residual leakage

$$\epsilon_L = v_L - \hat{v}_{L,\mathrm{SCA}} \tag{19}$$

which represents the incorrigible error introduced by leakage. After averaging to typical scatterometer product resolutions,

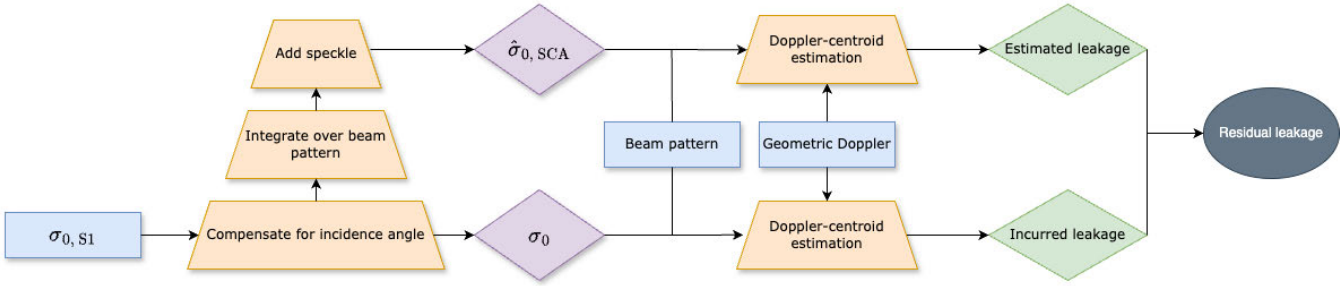

Fig. 3. Flowchart for the retrieval of estimated, incurred, and residual leakage; starting from the high-resolution NRCS, beam pattern, and geometric Doppler. For our symmetric beam and stationary surface, the estimated DC is the leakage.

the magnitude of residuals is in the order of $\mathcal{O}(0.1\ \mathrm{m \cdot s^{-1}})$, and locally up to $\mathcal{O}(1\ \mathrm{m \cdot s^{-1}})$. The power of these residuals is reduced at all scales with respect to the original leakage spectra, see Fig. 2, illustrating successful leakage reduction.

D. Pulse-Pair Measurement Uncertainty

Likely, the greatest velocity uncertainty of Doppler scatterometers results from the pulse-pair observation mechanism. We simulate and add this uncertainty so that it can be quantitatively compared with leakage velocity. Making the best estimates of pulse-pair uncertainties falls outside the scope of this study. Since the derivation is nontrivial, it is documented in Appendix A (with slight deviations from the literature).

Uncertainty can be reduced by averaging over independent samples. In the particular case of DopSCA, Hoogeboom et al. [19] used the equivalent number of independent samples present within a 25-km slant-range window, reducing LoS uncertainty to $\sim$1 $\mathrm{m \cdot s^{-1}}$. The wide spectral response of an unweighted 25-km moving-average operation is similar to that of a 50-km Hann low-pass filter, which we use in this study. Approximately 2-$\mathrm{m \cdot s^{-1}}$ instantaneous pulse-pair uncertainty can be expected at a ground-projected 50-$\mathrm{m \cdot s^{-1}}$ resolution for the considered range of incidence angles and based on an expected pulse-pair phase coherence of 0.39 estimated in Appendix A.

E. Case Studies

Several sequences of Sentinel-1 observations are used to emulate scatterometer scenes. We focus primarily on a longer sequence of successive observations near the Azores. Metadata for these case studies can be found in Appendix B.

In addition, we utilize a time series of observations made over the eastern Aghulas for which a dataset of surface-current estimates is available [11]. This dataset contains calibrated DC anomalies (DCAs) and estimates of the wind-wave Doppler. These are compensated to account for the differing incidence angles between Sentinel-1 and the synthesized scatterometer. The retrieved DCA is corrected for the estimated wind-wave Doppler and converted to a surface current. In turn, this current is interpolated to the $\sigma_{0,\mathrm{SCA}}$ coordinates and integrated over the beam- and backscatter-weighted footprint to the scatterometer's spatial resolution, yielding the OSC as would be observed by DopSCA: u_{OSC}.

III. Results and Discussion

The analyses presented in this section intend to assess the magnitude of uncertainty introduced by leakage velocity, our ability to correct for this uncertainty, and the implications of residual uncertainty on mission objectives. Results are presented as ground-projected velocities at a 50-km spatial resolution over the shared spatial extent.

A. Instantaneous Leakage Velocity and Correction

The Azores case study presents azimuthal NRCS gradients at varying scales [see Fig. 4(a) and (b)]. One can identify strong leakage in (c), wherever azimuthal inhomogeneities or trends in NRCS are present. Prevalent in particular is the bias of positive leakage toward the upper half of the domain.

With an RMSE of 1.20 $\mathrm{m \cdot s^{-1}}$, the uncertainty introduced by leakage would easily compare to the signal of strong surface currents. Correcting for leakage improves results: the RMSE of residual leakage in (d) drop to 0.38 $\mathrm{m \cdot s^{-1}}$ and the prevailing leakage bias has vanished. Using the coarse, scatterometer-observed NRCS, it is thus feasible to reduce the leakage uncertainty to $\mathcal{O}(0.1\ \mathrm{m \cdot s^{-1}})$.

For DopSCA, the presented instantaneous effect of leakage would be masked by the dominant instantaneous pulse-pair uncertainty, whose realization for this case study had an RMSE of 2.12 $\mathrm{m \cdot s^{-1}}$—about twice that of leakage. Nonetheless, the combined RMSE of leakage and pulse-pair uncertainty drops from 2.40 to 2.18 $\mathrm{m \cdot s^{-1}}$ after leakage correction. Thus, correcting for leakage shaves of several $\mathrm{dm \cdot s^{-1}}$ worth of errors. Systems capable of suppressing pulse-pair uncertainty would see an increased sensitivity to leakage and may even be dominated by it.

B. Temporal Persistence of Leakage

Residual leakage (and pulse-pair uncertainty) may be reduced further through temporal averaging. Since leakage is correlated with NRCS gradients, the stochastic behavior of these gradients determines the behavior of leakage. Currents are known to be long-lived and sources of NRCS gradients, so they might impart their temporal persistence onto the residual leakage. To then consider performance on a temporal scale, we next assess the persistence of residual-leakage with respect to a time series of surface-current observations.

The eastern Aghulas is characterized by a strong and relatively stable OSC (see Fig. 5). The rare availability of

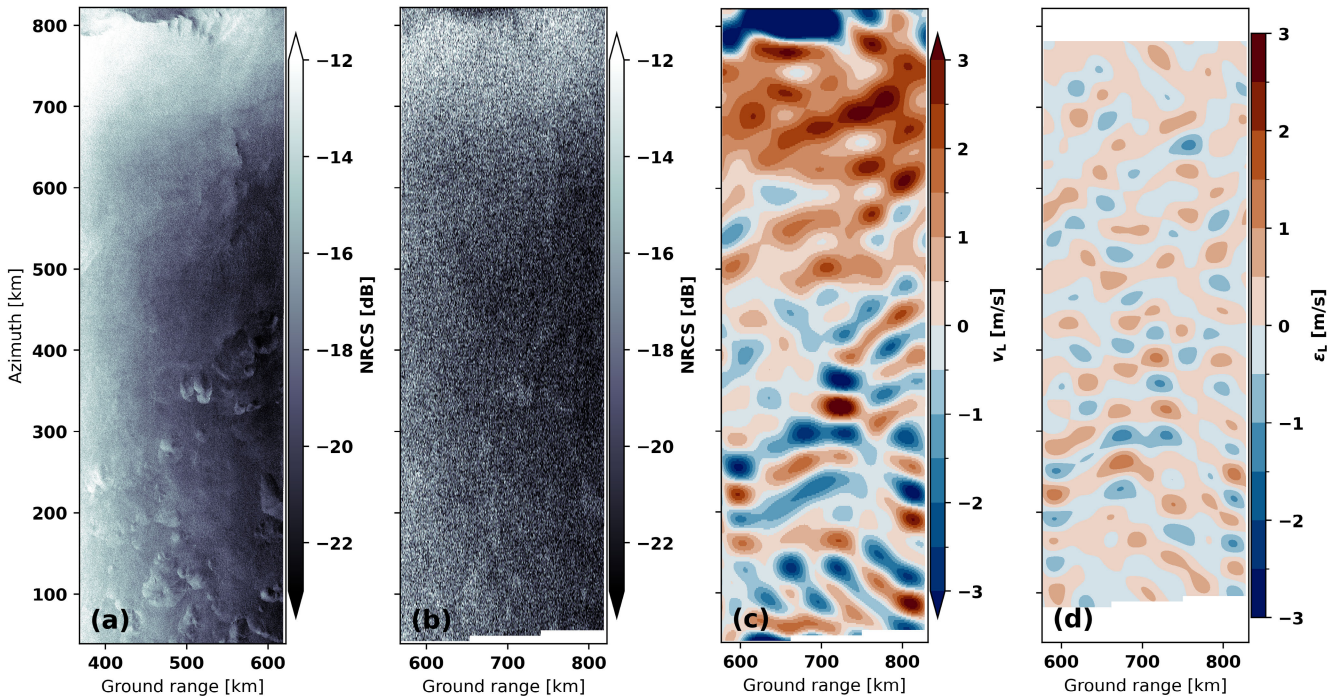

Fig. 4. Case study near the Azores of five stitched Sentinel-1B acquisitions taken on November 27, 2020 at 19:39. (a) Original Sentinel-1 $\sigma_{0,\mathrm{S1}}$, (b) synthesized scatterometer realization $\hat{\sigma}_{0,\mathrm{SCA}}$ where different viewing geometries with respect to Sentinel-1 results in a different equivalent ground-range coverage (azimuth is cropped due to beam integration extending outside of $\sigma_{0,\mathrm{S1}}$ domain), (c) incurred leakage velocity v_L, and (d) residual leakage velocity post correction ϵ_L. RMSEs for (c) and (d) are 1.20 and 0.38 m $\cdot$ s^{-1}, respectively, at a 50-km spatial resolution over their shared spatial extent.

TABLE II

VARIABILITY OF OSCS AND RESIDUAL LEAKAGE VELOCITY FOR THE AGHULAS CASE STUDY WHEN CONSIDERING AND OMITTING THE ADDITION OF SPECKLE TO THE SYNTHESIZED SCATTEROMETER NRCS FOR $N = 7$ SAMPLES. ONLY CONSIDERING DATA POINTS AVAILABLE ON ALL DATES. COLUMNS INDICATE AVERAGE TEMPORAL STANDARD DEVIATION $\langle\sigma_{u_{\mathrm{OSC}}}\rangle$, STANDARD DEVIATION OF THE TEMPORAL AVERAGE SURFACE CURRENT $\sigma_{\langle u_{\mathrm{OSC}}\rangle}$, AVERAGE TEMPORAL STANDARD DEVIATION OF RESIDUAL LEAKAGE $\langle\sigma_{\epsilon_L}\rangle$, AND STANDARD DEVIATION OF THE TEMPORAL AVERAGE RESIDUAL LEAKAGE $\sigma_{\langle\epsilon_L\rangle}$. ALL UNITS IN m s^{-1}

	$\langle\sigma_{u_{\mathrm{OSC}}}\rangle$	$\sigma_{\langle u_{\mathrm{OSC}}\rangle}$	$\langle\sigma_{\epsilon_L}\rangle$	$\sigma_{\langle\epsilon_L\rangle}$	$\langle\sigma_{\epsilon_L}\rangle/\sqrt{N}$
With speckle	0.44	0.33	0.45	0.21	0.17
No speckle	0.44	0.33	0.27	0.14	0.10

co-located and calibrated Doppler measurements over the Aghulas enables a relative comparison of leakage velocity with respect to the observed surface current.

To show that the OSC is persistent, we compare the mean standard deviation of the individual OSC images and the standard deviation of the mean. As shown in Table II, the mean standard deviation of OSCs over the seven presented days, $\langle\sigma_{u_{\mathrm{OSC}}}\rangle$, is 0.44 m $\cdot$ s^{-1}, and the standard deviation of the temporal mean OSC, $\sigma_{\langle u_{\mathrm{OSC}}\rangle}$, is 0.33 m $\cdot$ s^{-1}. Were the time series of OSCs uncorrelated in time, their standard deviation would decrease by the square root of the number of samples, in this case, a factor $\sqrt{7}$, to 0.17 m $\cdot$ s^{-1}. Unlike for the OSC, such a reduction is observed in the residual leakage velocity, whose mean standard deviation, $\langle\sigma_{\epsilon_L}\rangle$, is 0.45 m $\cdot$ s^{-1} while the standard deviation of the temporal mean $\sigma_{\langle\epsilon_L\rangle}$, is 0.21 m $\cdot$ s^{-1}. The latter is much closer to the 0.17 m $\cdot$ s^{-1} expected for an uncorrelated process (following $\langle\sigma_{\epsilon_L}\rangle/(N)^{1/2}$). Thus, despite significant temporal autocorrelation in OSCs, at the considered temporal scales, currents do not actually introduce persistent leakage. This, therefore, enables further reductions of the residual leakage through temporal averaging.

The lack of temporal autocorrelation in residual leakage may be explained by two compatible hypotheses: few of the unresolved NRCS gradients are caused by temporally persistent currents such that they impart little of their persistent nature onto the residuals, or leakage estimation and correction are inhibited by the random speckle present in the synthesized scatterometer NRCS. The first hypothesis is difficult to test as it requires precise knowledge of what NRCS is related to which phenomena. The second hypothesis is assessed by omitting the addition of speckle when producing synthetic scatterometer data. Summary results from this second analysis over the Aghulas are also presented in Table II. In the absence of speckle the residual leakage drops significantly from 0.45 to 0.27 m $\cdot$ s^{-1}. Nonetheless, the remaining signal still behaves as an uncorrelated random variable; the standard deviation of the temporal mean residual leakage at 0.14 m $\cdot$ s^{-1} approaches the expected 0.10 m $\cdot$ s^{-1} for an uncorrelated random variable. It then follows that the first hypothesis is likely responsible for the majority of the residual leakage's lacking temporal autocorrelation.

C. Implications to System Design

Given the above observations, we can consider what system design parameters ought to minimize exposure to residual

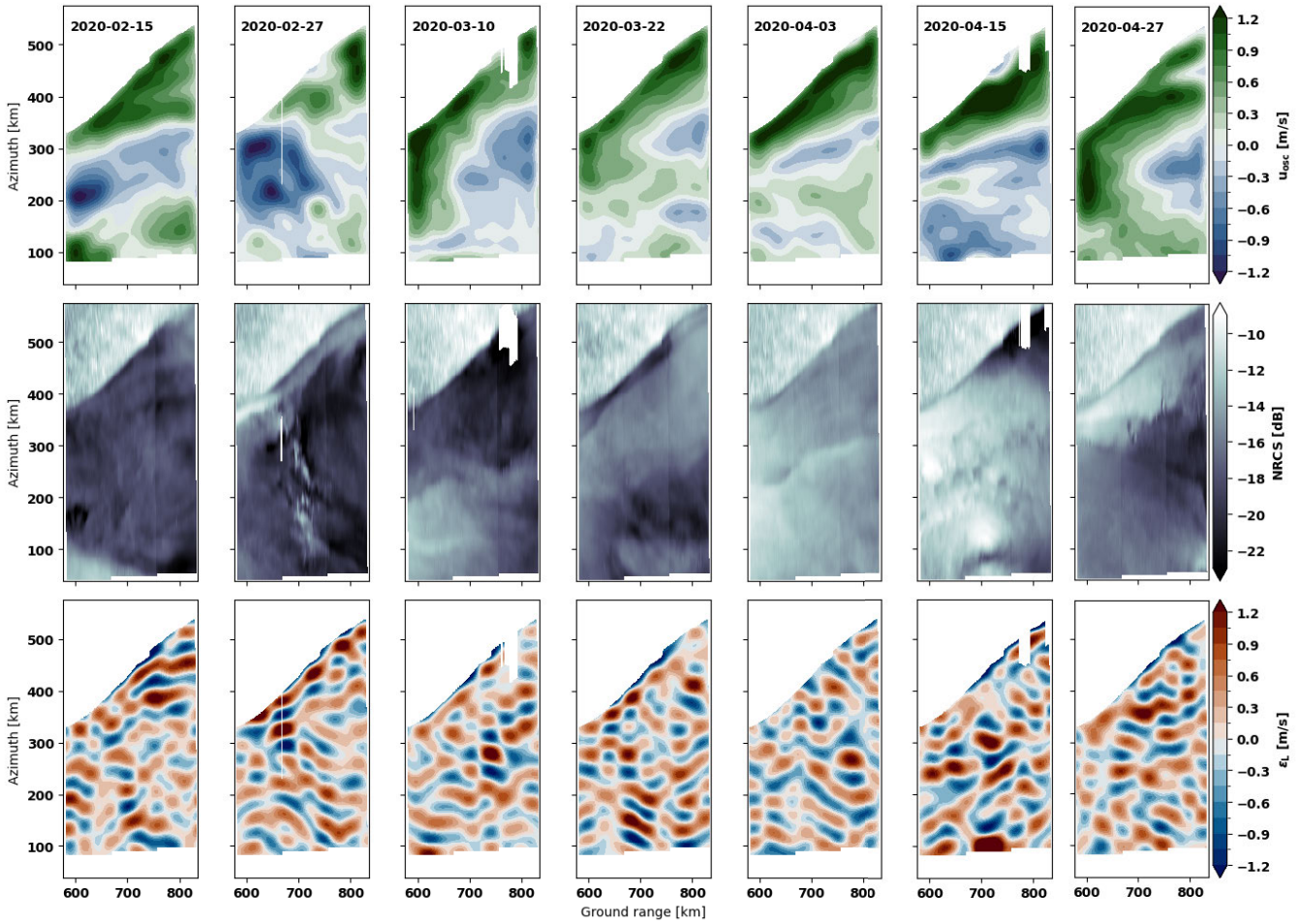

Fig. 5. (Top) Scatterometer $\sigma_{0,\mathrm{SCA}}$ (without the addition of speckle) at native resolution for a time series over the eastern Aghulas. (Middle) OSCs from Sentinel-1 integrated over the scatterometer beam at 50-km spatial resolution. (Bottom) Residual leakage velocity at 50-km spatial resolution.

leakage, focusing in particular on azimuthal resolution and the number of independent samples. The number of independent samples determines how much spatial averaging can be performed to reduce speckle's inhibitory effect on corrections, whereas the azimuthal resolution sets the sensitivity to the range of unsampled spatial frequencies. And, as observed from Fig. 2, smaller spatial scales contain less energy and can thus be expected to lead to less leakage.

To illustrate the relative importance of both aspects, we assess performances for the case studies listed in Table III with varying antenna lengths, which directly affects the azimuthal resolution. The number of independent samples can be enhanced by increasing the pulse bandwidth (yielding a greater range resolution) and PRF (yielding more samples in azimuth). Both options are computationally expensive to simulate. Instead, no speckle will be added for a run of analyses to simulate the effect of a sufficient number of independent samples capable of nullifying speckle in the limit.

These simulations, summarized in Fig. 6, corroborate results obtained for the Aghulas case, with a marked decrease in correction capabilities in the presence of speckle. A consistent exponential decay is observed. Such consistency permits the inference of performance for other Doppler scatterometers. For instance, at the same 50-km spatial resolution, pencil-beam

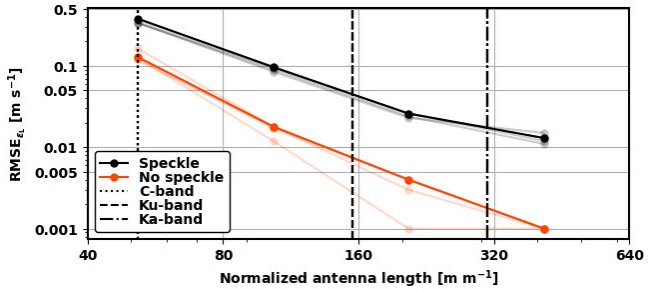

Fig. 6. Residual leakage for case studies as a function of wavelength-normalized antenna lengths. Reference values are indicated for C-, Ku-, and Ka-band systems assuming a tapered beam for a 2.87-m-long antenna. Performance for the Azores case is highlighted with the other case studies listed in Table III grayed out. The "no speckle" case represents the limit in residual-leakage reduction due to spatial averaging. A greater along-azimuth extent η and sampling is required to provide representative results outside the range of normalized antenna lengths between 40 and 640, respectively.

scatterometers operating at Ku band with a PRF in the kilohertz (kHz) range should expect a similar sensitivity to residual leakage as the equivalent DopSCA setup with no speckle (assuming that speckle reduction is enabled through the greater PRF) and a three times longer antenna. These results also illustrate limitations of conventional C-band scatterometer designs, as a kHz PRF may all but eliminate pulse-pair uncertainty and

speckle, yet residual leakage will remain significant (unless SAR processing is possible). Azimuthal resolution is thus the key parameter to target when aiming to mitigate leakage.

Other mitigation strategies could include narrowing the beam footprint by reducing its tapering. This lowers the sensitivity to NRCS gradients at the expense of reduced sidelobe suppression. Alternatively, a squinted viewing geometry could decrease the effective geometric-Doppler gradient and subsequent leakage. And, under highly favorable conditions, a squinted geometry would also enable leakage cancellation through sign reversal by combining observations from opposing squints, e.g., fore and aft. However, alterations to the viewing geometry and beam pattern are prone to conflict with other mission considerations.

IV. Conclusion

In this study, we assess the sensitivity to leakage velocity with the aim of answering whether this source of uncertainty could jeopardize the performance of Doppler scatterometers. A theoretical analysis does not yield a convenient expression, as leakage is the result of nonlinear processes. Therefore, an empirical analysis is performed instead, using emulated scatterometer observations.

Results indicate that, over the considered range of elevation angles and if uncorrected, the instantaneous leakage velocity for DopSCA-like sensors would lead to $\sim$1-m$\cdot$s^{-1} uncertainty in surface velocity estimates at a 50-m$\cdot$s^{-1} ground-projected spatial resolution. After correction—which consists of estimating the leakage from the observed $\hat{\sigma}_{0,\mathrm{SCA}}$ and the known geometric Doppler and beam pattern—the leakage uncertainty reduces to $\mathcal{O}(0.1\ \mathrm{m}\cdot\mathrm{s}^{-1})$. Sub $\mathcal{O}(0.1\ \mathrm{m}\cdot\mathrm{s}^{-1})$ performance is unlikely for any C-band RAR system due to the relatively large beam footprints.

Temporal averaging effectively further reduces the instantaneous residual leakage through a twofold process. First, temporal averaging reduces the speckle's inhibiting effect on the estimation and correction of leakage. Second, since residual leakage experiences little autocorrelation from potential current-NRCS interactions—which suggests that leakage-inducing NRCS gradients are primarily caused by imprints of the fast-decorrelating atmosphere—it too is reduced successfully through temporal averaging. This holds over the strong and persistent surface currents of the eastern Aghulas, but it may not transfer to other spatiotemporal domains or scales.

For DopSCA, leakage is a second-order effect compared with the dominant pulse-pair uncertainty. However, where pulse-pair uncertainty is effectively reduced by averaging over more independent samples, this is not the case for leakage velocity, making leakage particularly relevant for systems where pulse-pair uncertainty is successfully suppressed.

Future missions could minimize their exposure to leakage and its residuals by targeting adequate combinations of independent observation samples and azimuthal resolution. When design alterations are unfeasible due to specific constraints, e.g., resolution tradeoffs, power requirements, and other limitations, then temporal averaging remains a broadly applicable and effective mitigation strategy.

A. Pulse-Pair Uncertainty

We make three simplifying assumptions during the estimation of pulse-pair uncertainty: the signal-to-clutter ratio (SCR) is 1 since overlapping reflections from the first and second pulses yield, on average, equal amounts of clutter and signal (we ignore variations in SCR due to variations in NRCS); we assume a Gaussian beam footprint in the coherence terms despite assuming a tapered beam elsewhere; and we assume clutter dominates over other noise terms such that the coherence loss due to the signal-to-noise and clutter ratio (SNCR) can be approximated in the following equation [13], [27]:

$$\gamma_{\mathrm{SNCR}} = \frac{\mathrm{S}}{S+N+C} \approx \frac{\mathrm{SCR}}{1+\mathrm{SCR}}. \tag{20}$$

The platform motion during the pulse-pair interval, τ_p, leads to a relative motion of the scatterers contributing to the radar echo within a resolution cell. The resulting decorrelation is dependent on the ratio of τ_p over T_D, where the latter indicates the time it takes for the satellite to move half the length of its antenna. Following [13], this coherence can be approximated for a Gaussian beam footprint at broadside (mid-beam) by

$$\gamma_D \approx \exp\left[-\left(\frac{\tau_p}{T_D}\right)^2\right] \tag{21}$$

$$T_D = \left(\sqrt{2}kV_p\sigma_{\phi a}\right)^{-1} \tag{22}$$

where k is the wavenumber ($= 2\pi\lambda^{-1}$) and $\sigma_{\phi a}$ is the 3-dB beamwidth in the azimuth direction. For SCA, T_D will be in the order of $\mathcal{O}(10^{-1})$ ms, but greater than the 0.115-ms subpulse separation time τ_p.

The ocean surface also decorrelates between subpulses. This coherence loss depends on the sea state and its wave-motion correlation time, T_W. Similar to (21), it is given by

$$\gamma_{TW} = \exp\left[-\left(\frac{\tau_p}{T_W}\right)^2\right] \tag{23}$$

where T_W is approximated as follows [28], [29]:

$$T_W \approx 3.29\lambda U^{-1}. \tag{24}$$

For reasonable wind speeds U observed with a C-band system, T_W will be in the order of $\mathcal{O}(10^1)$ ms. This is much greater than either τ_p or T_D, making ocean surface decorrelation a minor source of coherence loss.

We approximate the total coherence as the product of the three components

$$\gamma \approx \gamma_{\mathrm{SNR}}\,\gamma_D\,\gamma_{TW} \tag{25}$$

yielding a γ of approximately 0.39. Since, $1-\gamma \not\approx 1$ we are prevented from using the Cramer–Rao bound for pulse-pair velocity uncertainty of [30], which is only valid in the high coherence limit [13]. Instead, we generate pulse-pair velocity uncertainty from the 1-look phase-difference probability density function (pdf) in the following equation [31]:

$$p(\psi) = \frac{\left(1-\gamma^2\right)\left[\left(1-\beta^2\right)^{\frac{1}{2}} + \beta(\pi - \arccos\beta)\right]}{2\pi\left(1-\beta^2\right)^{\frac{3}{2}}} \tag{26}$$

TABLE III
METADATA FOR CASE STUDIES EXCLUDING THE AGHULAS

Region	Platform	Date/Time	Product unique ID
Azores	S1B	2020-11-27T19:39	A07B, B01D, CA05, CE1B, E23C
Caribbean	S1A	2023-11-04T23:08	5B80, 75FE, FCE5
Hawaii	S1A	2020-11-06T04:23	40AB, 9158, B0E7, B3F4
Iceland	S1A	2023-11-07T18:49	026F, 03F2, B5DE
Scotland	S1A	2023-11-09T18:32	6D0B, B440, BAFB, CE72

where $p(\psi)$ is the pdf of phase differences valid between $-\pi < \psi \leq \pi$ and $\beta = \gamma \cos(\psi)$. The phase-difference pdf is converted to velocity in the following equation:

$$p(\sigma_{pp}) = p(\psi)\frac{1}{2k\tau_p}\frac{1}{\sin(\theta_i)} \tag{27}$$

where the additional sine term converts vectors from LoS to a ground-projected one. Similar to the addition of speckle, band-limited pulse-pair uncertainty is generated at the independent slant-range-spaced sample resolution, interpolated to grid spacing through zero-padding in the Fourier domain, and then interpolated back to the ground-range-projected grid spacing.

B. Case Studies

See Table III.

C. Data Availability

The analyses of this study are performed using Ground Range Detected Copernicus Sentinel-1 data 2020/2023 retrieved from ASF's API on March 3, 2024, processed by ESA. This data are accessed using Ifremer's open source xsar file reader [32]. Beam patterns were generated using https://gitlab.tudelft.nl/drama/drama. The CMOD5.N implementation was used from https://gitlab.tudelft.nl/drama/stereoid. Reference wind fields needed to run CMOD5.N were retrieved through ECMWF's ERA5 API [33]. Calibrated Doppler measurements from the Aghulas campaign were obtained from the ESA WOC Project [11]. A repository generating the results of this study is available at: https://github.com/owenodriscoll/DopSCA_leakage

ACKNOWLEDGMENT

The authors thank two anonymous reviewers for their helpful suggestions, as well as ESA, Paris, France, ECMWF, Reading, U.K., and Ifremer, France, for providing access to the data used in this study.

REFERENCES

[1] S. Tanelli, E. Im, S. L. Durden, L. Facheris, and D. Giuli, "The effects of nonuniform beam filling on vertical rainfall velocity measurements with a spaceborne Doppler radar," *J. Atmos. Ocean. Technol.*, vol. 19, no. 7, pp. 1019–1034, Jul. 2002.

[2] N. A. J. Schutgens, "Simulated Doppler radar observations of inhomogeneous clouds: Application to the EarthCARE space mission," *J. Atmos. Ocean. Technol.*, vol. 25, no. 1, pp. 26–42, Jan. 2008.

[3] P. Kollias, S. Tanelli, A. Battaglia, and A. Tatarevic, "Evaluation of EarthCARE cloud profiling radar Doppler velocity measurements in particle sedimentation regimes," *J. Atmos. Ocean. Technol.*, vol. 31, no. 2, pp. 366–386, Feb. 2014.

[4] A. J. Illingworth et al., "WIVERN: A new satellite concept to provide global in-cloud winds, precipitation, and cloud properties," *Bull. Amer. Meteorol. Soc.*, vol. 99, no. 8, pp. 1669–1687, Aug. 2018.

[5] S. N. Madsen, "Estimating the Doppler centroid of SAR data," *IEEE Trans. Aerosp. Electron. Syst.*, vol. 25, no. 2, pp. 134–140, Mar. 1989.

[6] B. Chapron, F. Collard, and F. Ardhuin, "Direct measurements of ocean surface velocity from space: Interpretation and validation," *J. Geophys. Res., Oceans*, vol. 110, no. C7, pp. 1–16, Jul. 2005.

[7] M. W. Hansen, F. Collard, K.-F. Dagestad, J. A. Johannessen, P. Fabry, and B. Chapron, "Retrieval of sea surface range velocities from ENVISAT ASAR Doppler centroid measurements," *IEEE Trans. Geosci. Remote Sens.*, vol. 49, no. 10, pp. 3582–3592, Oct. 2011.

[8] F. Ardhuin et al., "SKIM, a candidate satellite mission exploring global ocean currents and waves," *Frontiers Mar. Sci.*, vol. 6, p. 209, Apr. 2019.

[9] E. Rodríguez et al., "The winds and currents mission concept," *Frontiers Mar. Sci.*, vol. 6, p. 438, Jul. 2019.

[10] Y. Du et al., "Ocean surface current multiscale observation mission (OSCOM): Simultaneous measurement of ocean surface current, vector wind, and temperature," *Prog. Oceanogr.*, vol. 193, Apr. 2021, Art. no. 102531.

[11] *Sentinel-1 IW Ocean Surface Current Radial Velocity Over Agulhas Region From ESA WOC Project. Ver. 2.0*, NERSC, Plouzane, France, 2022.

[12] R. Morrow et al., "Global observations of fine-scale ocean surface topography with the surface water and ocean topography (SWOT) mission," *Frontiers Mar. Sci.*, vol. 6, p. 232, May 2019.

[13] E. Rodríguez et al., "Estimating ocean vector winds and currents using a Ka-band pencil-beam Doppler scatterometer," *Remote Sens.*, vol. 10, no. 4, p. 576, Apr. 2018.

[14] P. López-Dekker, H. Rott, P. Prats-Iraola, B. Chapron, K. Scipal, and E. D. Witte, "Harmony: An Earth explorer 10 mission candidate to observe land, ice, and ocean surface dynamics," in *Proc. IEEE Int. Geosci. Remote Sens. Symp. (IGARSS)*, Jul. 2019, pp. 8381–8384.

[15] R. Bamler, "Doppler frequency estimation and the cramer-rao bound," *IEEE Trans. Geosci. Remote Sens.*, vol. 29, no. 3, pp. 385–390, May 1991.

[16] G. Engen and H. Johnsen, "High-precision Doppler frequency estimation for ocean applications," *SeaSAR*, vol. 709, p. 14, Mar. 2013.

[17] G. Engen and H. Johnsen, *Sentinel-1 Doppler and Ocean Radial Velocity (RVL) Algorithm Definition*, document 19/2015, 2015.

[18] P. Fabry et al., "Feasibility study of sea surface currents measurements with Doppler scatterometers," *Currents*, vol. 240, nos. 50–100, p. 233, Dec. 2013.

[19] P. Hoogeboom, A. Stoffelen, and P. Lopez-Dekker, "DopSCA, scatterometer-based simultaneous ocean vector current and wind estimation," in *Proc. Doppler Oceanogr. Space*, Oct. 2018, pp. 1–9.

[20] R. K. Raney, "Doppler properties of radars in circular orbits," *Int. J. Remote Sens.*, vol. 7, no. 9, pp. 1153–1162, Sep. 1986.

[21] E. Peral, E. Rodríguez, and D. Esteban-Fernández, "Impact of surface waves on SWOT's projected ocean accuracy," *Remote Sens.*, vol. 7, no. 11, pp. 14509–14529, Nov. 2015.

[22] H. Hersbach, "CMOD5.N : A C-band geophysical model function for equivalent neutral wind," Eur. Centre Medium-Range Weather Forecasts, U.K., Tech. Rep. 554, 2008, doi: 10.21957/mzcfm6jfl.

[23] F. Fois, P. Hoogeboom, F. Le Chevalier, and A. Stoffelen, "DOPSCAT: A mission concept for a Doppler wind-scatterometer," in *Proc. IEEE Int. Geosci. Remote Sens. Symp. (IGARSS)*, Jul. 2015, pp. 2572–2575.

[24] F. Rostan, D. Ulrich, S. Riegger, and A. Østergaard, "MetoP-SG SCA wind scatterometer design and performance," in *Proc. IEEE Int. Geosci. Remote Sens. Symp. (IGARSS)*, Jul. 2016, pp. 7366–7369.

[25] I. G. Cumming and F. H. Wong, "Digital processing of synthetic aperture radar data," *Artech House*, vol. 1, no. 3, pp. 108–110, 2005.

[26] R. Gelsthorpe, E. Schied, and J. Wilson, "ASCAT-Metop's advanced scatterometer," *ESA Bull.*, vol. 102, pp. 19–27, Jun. 2000.

[27] E. Rodríguez and J. M. L. Martin, "Theory and design of interferometric synthetic aperture radars," *IEE Proc. F (Radar Signal Process.)*, vol. 139, no. 2, pp. 147–159, Jan. 1992.

[28] M. J. Tucker, "The decorrelation time of microwave radar echoes from the sea surface," *Int. J. Remote Sens.*, vol. 6, no. 7, pp. 1075–1089, Jul. 1985.

[29] S. Wollstadt, P. López-Dekker, F. De Zan, and M. Younis, "Design principles and considerations for spaceborne ATI SAR-based observations of ocean surface velocity vectors," *IEEE Trans. Geosci. Remote Sens.*, vol. 55, no. 8, pp. 4500–4519, Aug. 2017.

[30] M. S. Seymour and I. G. Cumming, "Maximum likelihood estimation for SAR interferometry," in *Proc. IEEE Int. Geosci. Remote Sens. Symp.*, Aug. 1994, pp. 2272–2275.
[31] J.-S. Lee, A. R. Miller, and K. W. Hoppel, "Statistics of phase difference and product magnitude of multi-look processed Gaussian signals," *Waves Random Media*, vol. 4, no. 3, pp. 307–319, Jul. 1994.
[32] O. Archer, A. Mouche, and A. Grouazel, "Xsar-synthetic aperture radar (SAR) level-1 grd Python mapper mapperfor efficient xarray/dask based processing," Ifremer, Plouzané, France, Tech. Rep., 2025. [Online]. Available: https://doi.org/10.12770/bd210be0-1d0b-4538-a2cd-a993de7431b0
[33] H. Hersbach et al., "ERA5 hourly data on single levels from 1959 to present," Copernicus Climate Change Service (C3S), Climate Data Store (CDS), ECMWF, U.K., Tech. Rep., 2023, doi: 10.24381/cds.adbb2d47.

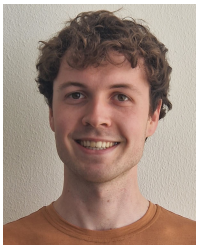

Owen O'Driscoll received the master's degree (cum laude) from the Faculty of Civil Engineering, Delft University of Technology, Delft, The Netherlands, in 2021, where he is currently pursuing the Ph.D. degree in radar oceanography with the Department of Geoscience and Remote Sensing.

From 2022 to 2023, he was with the Laboratory for Ocean Physics and Satellite remote sensing, Ifremer, Plouzané, France, to study air–sea interactions with spaceborne radars.

Paco López-Dekker (Senior Member, IEEE) was born in Nijmegen, The Netherlands, in 1972. He received the Ingeniero degree in telecommunication engineering from the Universitat Politècnica de Catalunya (UPC), Barcelona, Spain, in 1997, the M.S. degree in electrical and computer engineering from the University of California at Irvine, Irvine, CA, USA, in 1998, under the Balsells Fellowship, and the Ph.D. degree in clear-air imaging radar systems to study the atmospheric boundary layer from the University of Massachusetts, Amherst, MA, USA, in 2003.

In 2003, he joined Starlab Barcelona, Barcelona, where he worked on the development of Global Navigation Satellite Systems Reflectometry (GNSS-R) sensors and techniques. From 2004 to 2006, he was a Visiting Professor with the Department of Telecommunications and Systems Engineering, Universitat Autónoma de Barcelona, Bellaterra, Spain. He was awarded the Ramon y Cajal Grant to conduct pioneering research on bistatic synthetic aperture radar (SAR) at the Remote Sensing Laboratory, UPC, in March 2006. From November 2009 to August 2016, he was with the SAR Missions Group, Microwaves and Radar Institute, German Aerospace Center, Weßling, Germany. Since September 2016, he has been an Associate Professor with the Geoscience and Remote Sensing Department, Faculty of Civil Engineering and Geosciences, Delft University of Technology, Delft, The Netherlands. He has been deeply involved in the development of several radar missions and mission proposals and is the Lead Investigator of the Harmony European Space Agency (ESA), Paris, France, Earth Explorer 10 Mission. He has co-authored over 50 peer-reviewed journal articles and more than 125 conference contributions in a broad range of topics related to radar remote sensing.

Alexandre Payez received the master's degree in physics (summa cum laude) and the Ph.D. degree in astroparticle physics from the Université de Liége, Liége, Belgium, in 2007 and 2013, respectively.

He then worked with the Theory Group, Particle Accelerator and Fundamental Research Centre, DESY, Hamburg, Germany, as a Research Fellow of the Collaborative Research Centre SFB 676 "Particles, Strings and the Early Universe." In 2015, he became an ESA, Paris, France, Internal Research Fellow at European Space Agency (ESA), Darmstadt, Germany, where he worked on planetary defense against hazardous Earth-impacting asteroids, and also worked as part of the Mission Analysis Section on Mars Sample Return Carrier: a mission study together with NASA to bring back samples of Martian soil. He has been a Remote Sensing Researcher since 2019; first, he worked on the Earth's Radiation Budget at the Royal Meteorological Institute of Belgium (RMIB), Brussels, Belgium. He joined the Royal Netherlands Meteorological Institute (KNMI), De Bilt, The Netherlands, in 2021, to mainly work on the development of the ESA Earth Explorer 10 Mission Harmony, as part of the Harmony Science Team and the Infrared End-to-End Performance Simulator Team.